Materials Today Advances 17 (2023) 100355

Contents lists available at ScienceDirect

Materials Today Advances

journal homepage: www.journals.elsevier.com/materials-today-advances/

Heterojunction nanoarchitectonics of WO_x/Au-g-C_3N_4 with efficient photogenerated carrier separation and transfer toward improved NO and benzene conversion

Xiao Zhang [a], Katarzyna Matras-Postolek [a, *], Ping Yang [b, **]

[a] Faculty of Chemical Engineering and Technology, Cracow University of Technology, Warszawska 24 St, 31-155, Krakow, Poland
[b] School of Material Science & Engineering, University of Jinan, Jinan, 250022, PR China

ARTICLE INFO

Article history:
Received 26 December 2022
Received in revised form
8 February 2023
Accepted 9 February 2023
Available online 17 February 2023

Keywords:
G-C_3N_4 nanosheets
Au
WOx
Heterojunctions
NO and Benzene conversion

ABSTRACT

Topics on effectively improving the photochemical CO_2/benzene/NO oxidation conversion performances of g-C_3N_4 based materials via charge transfer and separation enhancement are still considered challenging, despite the growing popularity of applying these materials in a variety of energy conversion related applications. Based on the idea of nanoarchitectonics, a post-nanotechnology concept, WO_x/Au-g-C_3N_4 heterostructures are synthesized using two-step thermal polymerization and solvothermal treatment methods in this paper. Small Au nanoparticles are incorporated in superior thin g-C_3N_4 via mechano-chemical pre-reaction and two-step thermal polymerization (treated at 500 and 700 °C). Enhanced photocurrent density is observed after incorporation of Au, which is also in good agreement with the photocatalytic activity (H_2 generation and CO_2 reduction) data. Layered WO_x with abundant oxygen vacancies are further incorporated into Au-modified g-C_3N_4 nanosheets to form heterojunctions possessing excellent photocatalytic CO_2 photo-reduction performances with CO and CH_4 generation rate of 5.64 and 2.58 $\mu molg^{-1}h^{-1}$, respectively, under full solar spectrum. The heterojunctions constructed via in-situ formation show direct Z-scheme charge transfer pathway with improved charge separation and transport efficiencies. These highly stable and recyclable hierarchical g-C_3N_4 hybrid nanostructures (WO_x/Au-g-C_3N_4 heterojunctions) show outstanding conversion rate (88.1%) and selectivity (99.3%) for benzene to phenol conversion under full solar spectrum condition, as well as excellent NO removal rate (61%).

1. Introduction

Fossil fuel (involving coal, petroleum, heavy oils, natural gas etc.) combustion has been considered the primary cause for rising CO_2 and NO_x levels in the atmosphere that leads to anthropogenic climate change [1,2]. CO_2 has been generally believed to be one of the major contributors to the global warming by supercharging natural greenhouse effect; while NO_x emission been considered to be responsible for anthropogenic smog and acid rain formation. Techniques such as photocatalytic CO_2 and NO_x conversion, are promising choices that reduces atmospheric CO_2 and NO_x levels whilst reducing fossil fuel reliance in a sustainable way [3–5]. Various catalysis techniques involving electrocatalysis, photocatalysis, photoelectro-catalysis, and thermocatalysis, have been developed for converting CO_2 into valuable chemical fuels (e.g., methane, formaldehyde, methanol and other carbon-based fuels) [6–8]. During the conversion process, clean and sustainable energy source with high abundance (e.g., solar energy) as well as high-efficiency catalysts are often required to activate the quite stable CO_2 molecules, photocatalytic activation of CO_2 has been considered high potential choice [9–11].

Inspired by the natural photosynthesis, photocatalysis has been considered a promising energy conversion technology for converting CO_2 into solar fuels (e.g., carbon-based fuels), and H_2O is known to play a dominant role in these CO_2 photoreduction processes (involving light absorption step, charge separation process, and redox reaction process) [12]. Topics on the photocatalytic conversion of CO_2 and H_2O into carbon-based fuels using semiconductor catalysts have been widely studied [13–15]. Among a

* Corresponding author..
** Corresponding author.
E-mail addresses: k.matras@pk.edu.pl (K. Matras-Postolek), mse_yangp@ujn.edu.cn (P. Yang).

https://doi.org/10.1016/j.mtadv.2023.100355

variety of semiconducting photocatalysts, graphitic carbon nitride (g-C_3N_4) has been drawn considerable attention in photocatalytic solar energy conversion due to its high stability, nontoxicity and visible (Vis) light responsiveness [16–18]. Since g-C_3N_4 nanosheets are disadvantaged by its limited visible light absorption and high photogenerated charge carrier recombination rate in CO_2 conversion process, development of g-C_3N_4 based heterostructures with enhanced photocatalytic performances has become a quite popular topic [19–21]. The ordered unit arrangement and interlayer structure of C_3N_4 are often formed through pyrolysis of layered supramolecular precursors. The supramolecular layered precursors possess abundant functional groups (e.g., $-NH_2$ and $-OH$ in between heptazine layers) and large interlamellar distance that allows facile intercalation of small guest species (e.g., metal salts) forming heterostructures [11]. And tremendous efforts have been done on the optimization of these heterostructures to improve their photocatalytic performances for practical applications.

WO_3 having a band gap of around 2.6–2.9 eV has also been considered a high-performance visible-light-responsive photocatalyst [22–25]. However, the relatively lower conduction band (CB) edge position of WO_3 photocatalyst often leads to low reactivity towards photocatalytic CO_2 reduction and NO oxidation reactions as well as other photo-reduction/oxidation reactions. In order to improve the photogenerated charge carrier separation efficiency as well as the photocatalytic and electrochemical properties of WO_3 incorporated catalyst, oxygen vacancies can be introduced into WO_3 by defect engineering [26,27]. For example, specific cooling methods were utilized by Zhang et al. to introduce oxygen vacancies on exposed specific facets of WO_3 to attain improved photocatalytic oxidation activity [28]. Among a variety of WO_3 incorporated composites developed, two dimensional (2D)/2D heterostructures with the advantages of enlarged interfacial contact surface and improved charge carrier migration efficiency have been considered one of the most competitive choices. Although g-C_3N_4 based WO_3 2D/2D heterostructures have been widely studied for various photocatalytic applications (involving organic pollutants treatment, photocatalytic water splitting and CO_2 reduction etc.), development of high-performance g-C_3N_4/WO_3 based heterostructure catalysts still remains challenging.

For Z-scheme heterostructural system with multi-components, transport of photoexcited electrons occurs from the conduction band of catalyst component A to the valence band of catalyst component B, with photogenerated electrons and holes accumulated at the conduction band of component B and the valence band of component A, respectively [26,29,30]. And these photogenerated charge carriers often possess high reduction/oxidation capacity for photocatalytic reduction and oxidation in water splitting as well as CO_2 and NO_x conversion processes. In order to improve the charge transport efficiency in Z-scheme heterostructural system, deposition of metal nanoparticles has been an effective approach. The metal particles work as the electron acceptor for receiving electrons from the conduction band of the semiconductor photocatalyst. Among a variety of popular metal choices, gold as a plasmonic noble metal with surface plasmon resonance (SPR) effect, is the key for the photocatalytic activity enhancement of the heterostructure composites. The theory behind is that the enhanced localized electromagnetic fields and the SPR-induced plasmonic hot electrons are responsible for the enhanced interfacial charge carrier separation at the close contact of metal and semiconductor [31–33]. And by eliminating the potential interfacial charge transport barrier commonly encountered in type II heterostructure composites via Z-scheme heterostructure construction, improvement in charge separation efficiency and photocatalytic activity of these Au nanoparticles incorporated g-C_3N_4 based Z-scheme composite catalyst can be achieved.

Attention has been paid to the photocatalytic removal of NO (one of the most hazardous constituents in the NO_x gases family) and benzene-to-phenol conversion utilizing semiconducting catalysts in recent years, due to the high potentials of semiconductor catalysts in photocatalytic energy conversion and pollutants treatment applications [31–34]. Hydroxylated aromatic compounds (e.g., phenol) are often used as precursors or intermediates for the fabrication of plastic resins, dyes, and fibers in commercial and industrial scale. Phenol production in industrial scale often involves partial oxidation of isopropyl benzene via the high-energy consuming cumene process with acetone produced as the byproduct accompanied by an extremely low phenol yield of about 5%. It is thus imperative to develop more environmental-friendly alternative methodologies for benzene production. Solar energy conversion utilizing low-loading noble metal (Au in this case) modified carbon-based photocatalysts has been given special attention, because of the extremely high catalytic activity of Au and also due to the fact that the high chemical/thermal stability as well as the large surface area makes layered g-C_3N_4 a compelling base material for visible-light-driven benzene/NO_x oxidation [33].

As a trending post-nanotechnology concept, nanoarchitectonics (first introduced by Aono and co-workers in 2000) based on the idea of construction of multifunctional nanomaterials via combining/coupling different functional nanomaterials, has been drawing growing attention in nanofabrication recent years [35–38]. In this paper, a WO_x and Au modified g-C_3N_4 heterostructure having enhanced photochemical properties was constructed using the idea of nanoarchitectonics. Mechano-chemical treatment and thermal condensation process (on bulk g-C_3N_4 precursor) plays the key role in successful incorporation of homogeneously distributed small Au nanoparticles (NPs) and Au clusters in ultrathin g-C_3N_4 nanosheets. A 2D/2D WO_x/Au/g-C_3N_4 Z-scheme heterostructure was formed via in situ growth of WO_x nanobelts on Au modified g-C_3N_4 using solvothermal treatment method. Characterization techniques such as transmission electron microscopy (TEM), X-ray photoelectron spectroscopy (XPS), and Raman spectroscopy were applied to investigate the composition, microstructures, and photocatalytic mechanism of these heterostructures. Excellent photocatalytic CO_2 reduction performances (5.64 $\mu molg^{-1}h^{-1}$ for CO and 2.58 $\mu molg^{-1}h^{-1}$ for CH_4 generation) were observed for the WO_x/Au/g-C_3N_4 Z-scheme heterostructures. In addition, outstanding conversion rate (88.1%) and selectivity (99.3%) for benzene to phenol conversion under full solar spectrum condition, as well as excellent NO removal rate (61%) were created using these heterostructures.

2. Experimental section

Chemicals and preparation of Au/g-C_3N_4. Chemicals involving chloroauric acid ($AuClO_3$, 97%, as Au source), ascorbic acid (AA), tungsten hexachloride (WCl_6), melamine, Nafion solution, rhodamine (RhB), and ethanol were purchased from Sigma Aldrich and used with no further purification. The pristine ultrathin g-C_3N_4 nanosheets (sample CN) with no Au incorporation (for comparison uses) was synthesized via a two-step calcination process using one of our previously reported methodologies [16–18]. Mechano-chemical pre-treatment and multi-step thermal polymerization process (at high temperature settings) were used to fabricate Au modified g-C_3N_4 (Au–CN). Bulk g-C_3N_4 (as the precursor for Au–CN composite sample synthesis) was prepared via thermal polymerization of melamine at 500 °C. Certain amount of $AuClO_3$ were added to the bulk g-C_3N_4 base to reach the weight percentage of 0.5, 1.0, and 1.5 wt% for sample Au–CN-1, Au–CN-2, and Au–CN-3, respectively (as shown in Table 1). These precursor mixtures were ground with ethanol to dry before undergoing calcination process

Table 1
Preparation conditions used for sample synthesis.

Sample	Composition	$AuClO_3$(wt%)[a]	WCl_6(wt %)[a]	Procedure
CN	g-C_3N_4	0	0	Two-step synthesis
Au−CN-1	Au/g-C_3N_4	0.5	0	Pre-reaction
Au−CN-2	Au/g-C_3N_4	1.0	0	Pre-reaction
Au−CN-3	Au/g-C_3N_4	1.5	0	Pre-reaction
W−Au−CN-1	WO_x/Au/g-C_3N_4	1.0	6.0	Pre-reaction
W−Au−CN-2	WO_x/Au/g-C_3N_4	1.0	8.0	Pre-reaction
W−Au−CN-3	WO_x/Au/g-C_3N_4	1.0	10.0	No pre-reaction

[a] The weight ratio of $AuClO_3$ and WCl_6 to g-C_3N_4 used for sample preparation.

(in inert gas environment) in tube furnace (at 700 °C for 2 h, with a ramp rate of 5 °C/min) to obtain sample Au−CN-1, Au−CN-2, and Au−CN-3.

Preparation of WO_x/Au-g-C_3N_4 heterojunctions. WO_x modified Au/g-C_3N_4 heterojunctions were constructed using sample Au−CN-2 as the base precursor. To investigate the effects of WCl_6 (W source) on heterojunction formation, different amount of WCl_6 were mixed with Au/CN-2 to reach a weight percentage of 6.0, 8.0, and 10 wt% (for sample W−Au−CN-1, W−Au−CN-2, and W−Au−CN-3, respectively). 30 mL of ethanol was added to these powder mixtures followed by 5 min of sonication treatment. Scarce amount of AA was added to the obtained mixture (with a WCl_6 to AA molar ratio of 1:2 and constant stirring) followed by 20 min of stirring. The obtained suspension was then heat-treated in an oven at 220 °C for 10 h and washed with ethanol.

Material characterization. Transmission electron microscope (TEM, FEI Titan G2 80−200 TEM/STEM, FEI company) was used to collect the TEM and HAADF-STEM images of the Au−CN and W−Au−CN heterostructure samples. X-ray diffraction (XRD) patterns and the XPS spectra of the heterostructure samples were recorded using Bruker D8 X-ray diffractometer and Kratos Axis Ultra DLD spectrometer, respectively. UV−Vis diffuse reflectance and absorbance measurements were done on the heterostructure samples utilizing UV−Vis spectrophotometer (U-4100, Hitachi, Japan).

Photocatalytic CO_2 reduction. A mixture solution containing 20 mg of the heterostructure sample and 15 mL of deionized water was prepared for CO_2 photoreduction measurement. 20 min of high-purity CO_2 bubbling was done on the solution before vacuum treatment and conducting measurements under full solar spectrum irradiation (utilizing a LED light source). A GC-7920 gas chromatograph was used for recording and analyzing the data collected at certain time intervals.

Photocatalytic NO removal. A device having a cylindrical reaction chamber connected to a NO_x analyzer and a NO compression cylinder was used for photocatalytic NO oxidation measurements (at room temperature with a NO gas (600 ppb) flow rate of 1.2 mL/min). A quartz glass sheet with 0.1 g of heterostructure sample was placed onto the bottom plate of the cylindrical reaction chamber followed by exposing to 25 min of NO gas flow under no light irradiation condition (in order to reach the NO adsorption-desorption equilibrium with an initial NO concentration of C_0). 20 min of measurements were done on each sample under full solar spectrum irradiation condition (500 W Xe lamp as the light source) with the NO removal rate of the sample calculated using the following equation: $\left(1-\frac{C}{C_0}\right)\times 100\%$. Cyclic NO oxidation stability test was also performed on the heterostructure samples in full solar spectrum condition having the light source (Xe lamp) turned off at the end of each cycle and with the duration of each cycle been about 8 min. In order to examine the active species in the photocatalytic NO oxidation reactions, quenching experiments were performed on the heterostructure samples. 2 mmol of the scavengers (benzoquinone (BQ), $AgNO_3$, isopropanol (IPA), and ethylenediaminetetraacetic acid disodium salt (EDTA-Na_2)) and 0.1 g of the catalyst sample were dispersed in 5 mL of ethanol to obtain a mixture solution followed by 5 min of sonication. The obtained suspension was then coated and dried on quartz glass sheets before testing.

Photocatalytic oxidation of benzene. A catalyst suspension containing 10 mg of the catalyst sample, 1 mL of benzene, 5 mL of CH_3CN (as solvent) and 2 mL of 25% H_2O_2 was prepared and placed 10 cm from the light source. The benzene hydroxylation test was performed on the samples in a sealed environment under full solar spectrum irradiation for 12 h (at 50 °C). Gas chromatography mass spectrometry (GC-MS) and GC were used for collecting and analyzing the data. Phenol yield was calculated by dividing the phenol generated (mole) by the initial mass of benzene (mole), and the selectivity to phenol was calculated using the equation below.

$$\text{Selectivity to Phenol} = \frac{\text{phenol generated (mole)}}{\text{phenol} + \text{benzoquinone generated (mole)}} \times 100\%$$

Photocatalytic hydrogen generation and RhB degradation. A testing system having glass-closed gas circulation and Pyrex top-irradiation reaction vessel was used for photocatalytic hydrogen generation measurements. 25 min of sonication was done on the sample mixture containing 10 mg of the sample and 100 mL of triethanolamine solution (with a triethanolamine: deionized water volume ratio of 1:9) before removing air from the testing system. H_2 generation measurements were performed with constant stirring utilizing 300 W Xe lamp as the light source and argon as the Carrier gas. Shimadzu GC-7920 gas chromatography was used for data collection.

RhB photodegradation measurements utilizing 10 mg/L RhB solution were done on the heterostructure samples. A wavelength cut-off filter equipped 300 W Xe arc lamp was used as the light source. The active species in the RhB photodegradation process in full solar spectrum irradiation condition were investigated by adding scavengers in the catalyst sample solution (e.g., 0.0216 g of BQ, 0.034 g of $AgNO_3$, 2 mL of IPA, and 0.0744 g of EDTA-Na_2 were

mixed with 35 mL of mixture solution containing catalyst sample and RhB solution). A Bruker model ER200-SRC spectrometer was used for recording the ESR signals of the superoxide and hydroxyl radical adducts of 5,5-dimethyl-1-pyrroline *N*-oxide (DMPO).

3. Results and discussion

Scheme 1 shows the preparation procedure utilized on synthesizing WO_x/Au-g-C_3N_4 heterostructure samples based on the concept of nanoarchitectonics. Melamine was used as the precursor to synthesize bulk layered g-C_3N_4 consisted of melem building blocks (involving tri-*s*-triazine (C_6N_7) and triazine (C_3N_3) units) via thermal condensation process at 500 °C [39]. These layered g-C_3N_4 has π-conjugated system containing sp^2 hybridized carbon and nitrogen. A mechano-chemical pre-reaction treatment was required for mixing bulk g-C_3N_4 and the Au sources. The presence of abundant N sites in the g-C_3N_4 nanosheets is able to promote the incorporation of Au ions on g-C_3N_4 forming reaction sites so that Au can be anchored into the composite system during thermal polymerization process [24]. The Au nucleation and growth were triggered by the reduction of Au ions during the multi-step thermal polymerization process at 700 °C, leading to successful incorporation of Au clusters in superior thin g-C_3N_4 nanosheets substrate. Solvothermal treatment method was used to achieve in situ growth of WO_x nanobelts on the Au modified g-C_3N_4 base at 200 °C. The detailed preparation conditions used for synthesizing each sample are illustrated in Table 1.

Fig. 1a shows the scanning electron microscopy (SEM) image of pristine g-C_3N_4 with nanosheets morphology obtained via two-step thermal polymerization, while Fig. 1b to f shows the TEM images of sample Au−CN-2 (Au modified g-C_3N_4 prepared using a metal source weight percentage of 1%) at different magnifications. No obvious chunky Au NPs were observed for sample Au−CN-2, and the high-resolution TEM images of the Au clusters area of Au−CN-2 were recorded with the metal clusters circled in Fig. 1d to f. Moreover, the nanosheets morphology of g-C_3N_4 was maintained after Au loading, however the crystallinity of the g-C_3N_4 nanosheets was enhanced, and this can be attributed to the multi-step thermal polymerization process utilized for Au cluster incorporation. The observed lattice fringes with a spacing of 0.32 nm corresponding to the (002) facet of g-C_3N_4 (as observed on Fig. 1d to 1f) confirms the successful formation of g-C_3N_4 nanosheets.

Fig. 1g to j showed the high-angle annular dark-field scanning TEM (HAADF-STEM) images and elemental mapping (of N, C, and Au) for sample Au−CN-2. Homogeneously distributed Au with no obvious chunky Au NPs were observed for sample Au−CN-2, which also further confirms the successful embedment of Au clusters in Au−CN-2. However, as the weight percentage of metal source increased to 1.5% (sample Au−CN-3), small Au NPs with diameters of less than 6 nm were observed on the TEM images due to the increased Au loading (as shown in Fig. 1k, m, and 1n). According to literature, the lattice spacing of 0.23 nm observed on Fig. 1n corresponds to the (111) facet of Au [40].

The WO_x and Au modified sample W−Au−CN-1 still showed nanosheets morphology as shown in the SEM image of W−Au−CN-1 in Fig. 2a. Fig. 2b to d shows the TEM images of sample W−Au−CN-1 (at different magnifications) with limited amount of layered WO_x nanobelts and no obvious chunky Au NPs observed on Fig. 2b and c. Some of the Au clusters (incorporated in the W−Au−CN-1 composite system) were also circled in Fig. 2d. The interplanar spacing of 0.38 nm shown in the inset in Fig. 2b coincides with the (010) lattice of WO_3.

Moreover, the HADDF image and the elemental mapping (for N, C, Au, and W) of sample W−Au−CN-1 are shown in Fig. 2e to i, confirming successful incorporation of Au and WO_x in the heterostructure system. The TEM images of sample W−Au−CN-2 (with higher W source loading) were also collected for comparison (Fig. 2j, k, and 2m). Typical WO_x nanobelts are clearly observed in Fig. 2j and k. Compared with sample W−Au−CN-1, the amount of WO_x incorporated in W−Au−CN-2 increased, due to the fact that the amount of WO_x nanobelts observed on the surface of the sample W−Au−CN-2 (Fig. 2j) was much higher than that observed on W−Au−CN-1 (Fig. 2b). Well-developed lattice fringes with a 0.38 nm spacing corresponding to the (010) facet of WO_3 were also observed on sample W−Au−CN-2 as shown in Fig. 2m. As the amount of W sources added into the composite system increases, the amount of WO_x nanobelts grown along the surface of Au-g-C_3N_4 nanosheets also increases.

To analyze the composition of the WO_x and Au modified g-C_3N_4 based heterostructure samples, XPS measurements were performed on sample W−Au−CN-1 with the lowest amount of Au and WO_x incorporated among all the WO_x and Au modified heterostructure samples, and the XPS results are illustrated in Fig. 3. The C1s spectrum with the *C*−C (284.8 eV), *C*−OH (286.4 eV), O−C=O (288.9 eV), *C*−N/C=O (288.2 eV) components and a satellite peak at 293.5 eV are shown in Fig. 3a. Peaks at 298.5, 399.4 and 400.9 eV in the N 1s spectrum in Fig. 3b were assigned to pyridinic-N, pyrrolic N and graphitic N respectively, among which the pyridinic N and

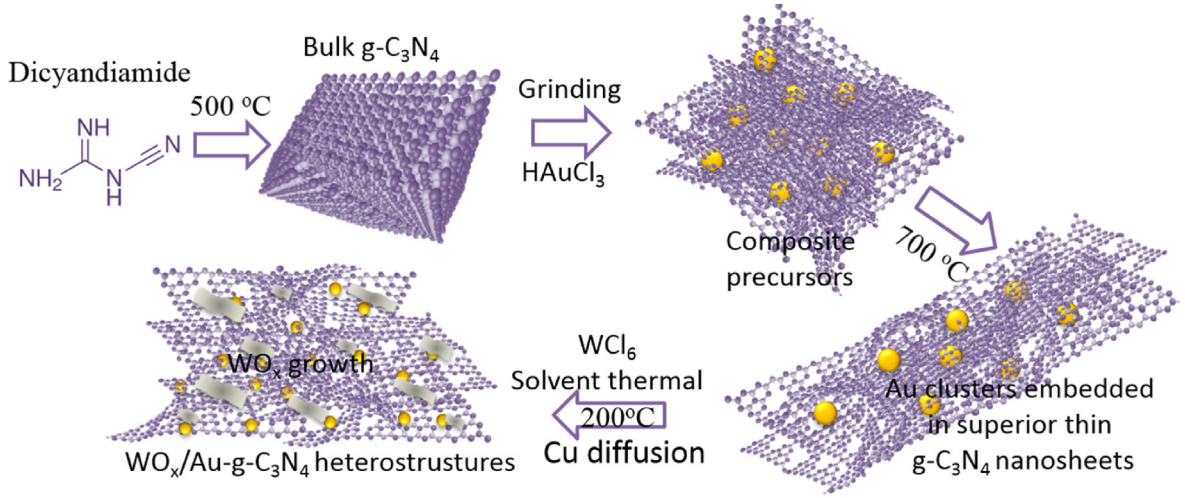

Scheme 1. Construction process of WO_x and Au modified g-C_3N_4 heterostructures using the idea of nanoarchitectonics.

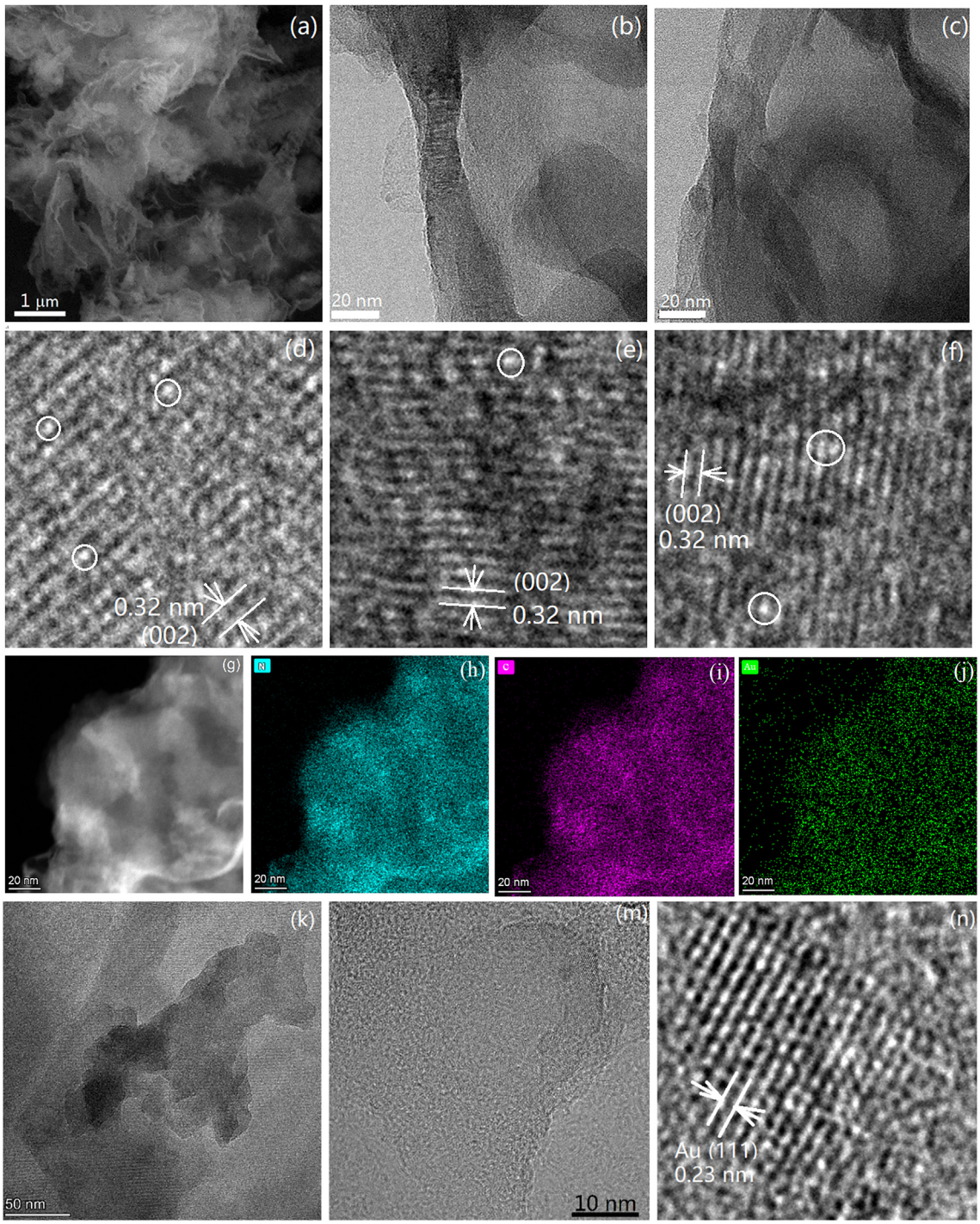

Fig. 1. (a) SEM image of sample CN (g-C_3N_4). (b to f) TEM images of sample Au–CN-2 at different magnification. (g to j) HADDF image and elemental mapping (N, C, Au) of sample Au–CN-2. (k, m, n) TEM images of sample Au–CN-3 at different magnification. The Au clusters incorporated into the composite system are circled in (d) to (f).

graphitic N were the two main N components and also the key factors that increased the number of active sites and promoted the nucleation of WO_x nanocomposites in the heterostructure sample. The W4f spectrum in Fig. 3c was fitted into five peaks. The two relatively small peaks at 33.9 and 36.1 eV are attributed to the $W4f_{7/2}$ and $W4f_{5/2}$ peaks of W^{5+} state, respectively, whereas the two large peaks at 35.3 and 37.6 eV correspond to that of the W^{6+} state [41]. By creating more oxygen vacancy defects in the WO_x modified Au-g-C_3N_4 layered heterostructure system (confirmed by the observation of W^{5+} and W^{6+} states in the W4f spectrum), the charge carrier separation efficiency and thus the photocatalytic performances of the WO_x modified heterostructure catalysts can be enhanced. The O1s spectrum of sample W–Au–CN-1 in Fig. 3d was fitted into three peaks with oxide (at 530.1 eV with the highest peak intensity) originated from WO_3 in the composite system to be the main component [42]. The peak at 531.5 eV corresponds to the hydroxide species in the composite system while the peak at 532.8 eV can be attributed to the adsorbed organics/H_2O species in

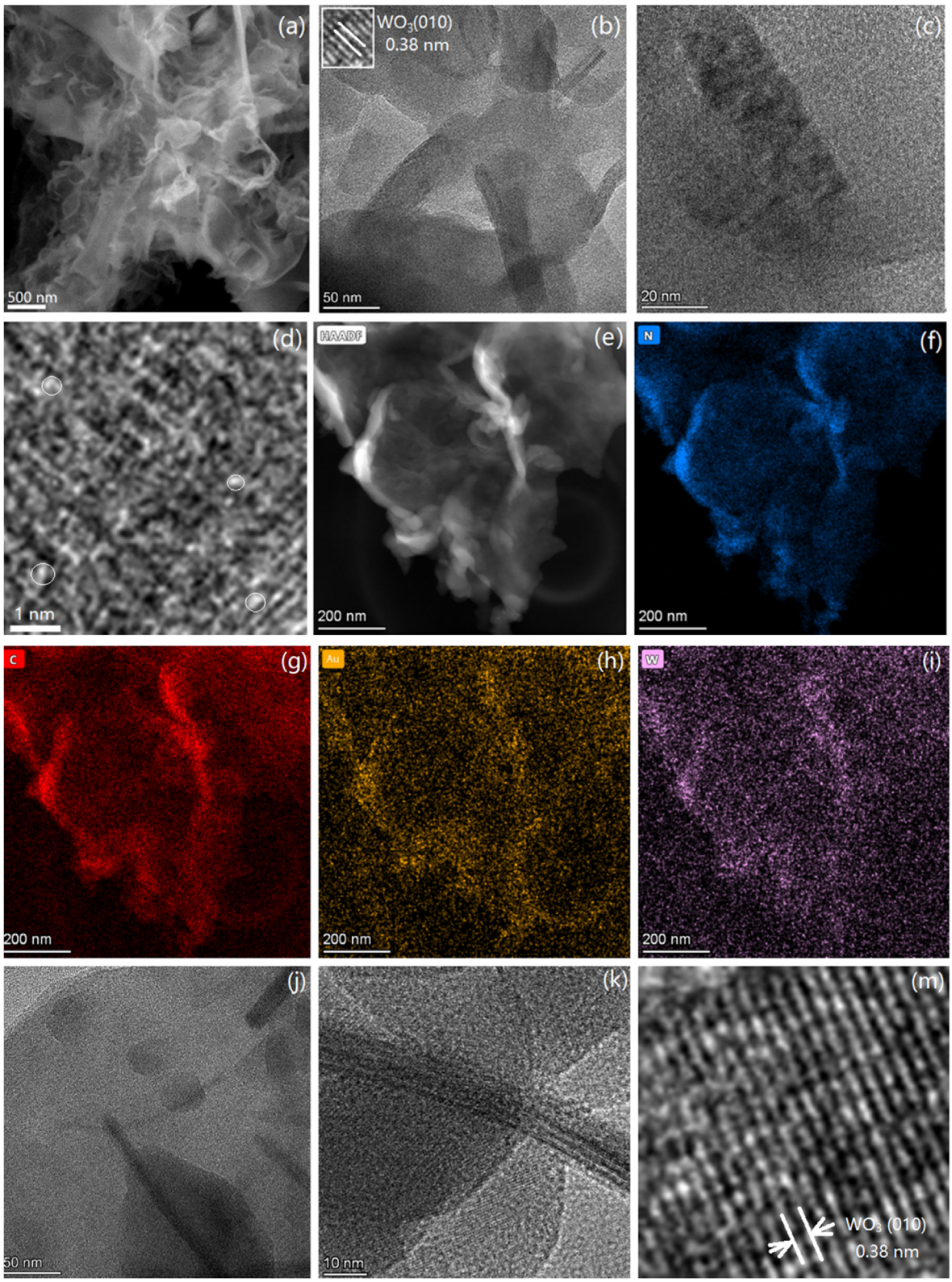

Fig. 2. (a) SEM image of sample W–Au–CN-1. (b to d) TEM image of sample W–Au–CN-1 at different magnification. (e to i) HADDF image and elemental mapping (N, C, Au, W) for sample W–Au–CN-1 with Au clusters circled in (d). (j, k) TEM images of sample W–Au–CN-2. (m) And the inset in (b) show a lattice spacing of 0.38 nm corresponding to the (010) facet of WO_3.

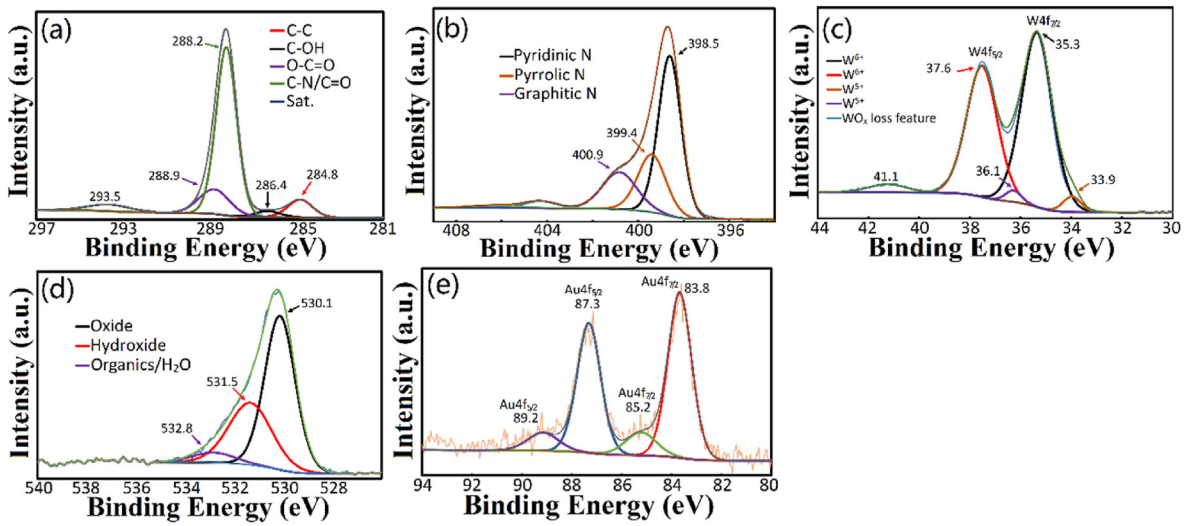

Fig. 3. XPS spectra of sample W–Au–CN-1: (a) C 1s spectrum; (b) N 1s spectrum; (c) W 4f spectrum; (d) O 1s spectrum; (e) Au 4f spectrum.

the sample. Fig. 3e shows the Au 4f spectra of the heterostructure composites W–Au–CN-1. The two peaks located at 83.8 and 85.2 eV correspond to the Au $4f_{5/2}$ peaks while the peaks at 87.3 and 89.2 eV are related to the Au $4f_{7/2}$ peaks [43].

To further investigate the composition of the composite samples, XRD measurements were performed on Au modified g-C_3N_4 (sample Au–CN-2) and the WO_x incorporated Au–CN-2 (sample W–Au–CN-2) as illustrated in Fig. 4a. Both Au–CN-2 and W–Au–CN-2 showed diffraction peaks corresponding to the (100) and (002) facets of g-C_3N_4 and the characterisitic peaks of Au, which also confirms the successful incorporation of Au into the heterostructure system. The relatively low intensity of Au peaks observed in the XRD pattern of sample Au–CN-2 and W–Au–CN-2 can be attributed to the fact that the amount of Au introduced into the composites system was scarce. The peak intensity of g-C_3N_4 related peaks remained almost unchanged after WO_x modification, which indicates that the primary structure of g-C_3N_4 nanosheets was maintained after WO_x immobilization. Moreover, three WO_3 phase peaks and one WO_2 phase peak were observed on the XRD pattern of sample W–Au–CN-2 in Fig. 4a, suggesting that WO_3 was the main WO_x species in sample W–Au–CN-2 and that only limited amount of WO_2 was formed in the composite system. These results also matched with the XPS data obtained. The presence of both WO_3 and WO_2 phases in the W–Au–CN-2 composite system confirms the formation of surface oxygen vacancies in W–Au–CN-2 heterostructure system, with the addition of reducing agents during the solvothermal treatment process been the key for defect engineering in this case.

Photocurrent and UV–Vis diffuse reflectance measurements were also performed on sample Au–CN-2 and W–Au–CN-2, and the data are shown in Fig. 4b and c. It was obvious that the photocurrent intensity of pristine g-C_3N_4 nanosheets increased drastically after Au cluster incorporation (as illustrated in Fig. 4b) because of the drastically enhanced conductivity in the presence of Au in the composite system. And a further increase in photocurrent intensity was also observed after WO_x nanobelts immobilization on Au–CN-2, indicating the successful formation of W–Au–CN-2 heterostructures. In case of UV–Vis diffuse reflectance spectra data shown in Fig. 4c, the diffuse reflectance spectrum of the composite sample (Au–CN-2) remained almost unchanged after Au cluster incorporation, however, a drastic change in the spectrum was observed for the WO_x modified Au–CN-2 heterostructures (sample W–Au–CN-2). This can be attributed to the small particle size of the Au clusters. These incorporated Au clusters show enhanced absorption band near blue light region in this case. The extension in light absorption (to the visible/near infrared and full solar spectrum) range, band-to-band transitions, as well as band gap narrowing effects observed for the heterostructure sample W–Au–CN-2 were the keys in improving photocatalytic activity of the heterostructure catalysts [44].

UV-excited Raman measurements were done on pristine g-C_3N_4, Au–CN-2, and W–Au–CN-2 sample with the results shown in Fig. 4d. The pristine g-C_3N_4 nanosheets sample showed a typical g-C_3N_4 Raman spectrum with relatively lower intensity. An increase in peak intensity was observed for the Au clusters modified g-C_3N_4 (sample Au–CN-2), indicating the successful embedment of Au during the thermal polymerization treatment stage. The mechanochemical pre-treatment done on the Au source and g-C_3N_4 nanosheets base before thermal polymerization process was also the key for achieving successful incorporation of Au ions into the g-C_3N_4 framework forming a highly ordered structure. The WO_x immobilized sample (W–Au–CN-2) has similar peak positions as that of sample Au–CN-2, but higher peak intensity. This can be attributed to the presence of highly ordered structure of the W–Au–CN-2 heterostructure (maintained even after WO_x modification) and also due to the interplay among the different components (g-C_3N_4, Cu, and WO_x) in the composite system. Moreover, the additional peaks observed for the Au and Au/WO_x modified composite sample (highlighted using asterisk for sample W–Au–CN-2 and using a circle for sample Au–CN-2 in Fig. 4d) also confirmed the interplay in-between g-C_3N_4, Au, and WO_x.

To evaluate the photocatalytic performances of the heterostructure samples, photocatalytic hydrogen generation and CO_2 photo-reduction measurements (under full solar-spectrum condition, without using any co-catalysts) were performed on the catalyst samples, and the results are illustrated in Table 2. Sample Au–CN-2 showed the highest H_2 generation rate (560 $\mu molg^{-1}h^{-1}$) among the three Au modified g-C_3N_4 samples (Au–CN). And sample W–Au–CN-2 with optimized Au and W source ratio revealed the highest H_2 evolution activity among all the seven samples listed in Table 2, which is about 10 times of that of sample Au–CN-2. The H_2 generation rate measured for the WO_x immobilized sample W–Au–CN-1, W–Au–CN-2, and W–Au–CN-3 were 3990, 5659, and 4100 $\mu molg^{-1}h^{-1}$, respectively. A significant improvement in

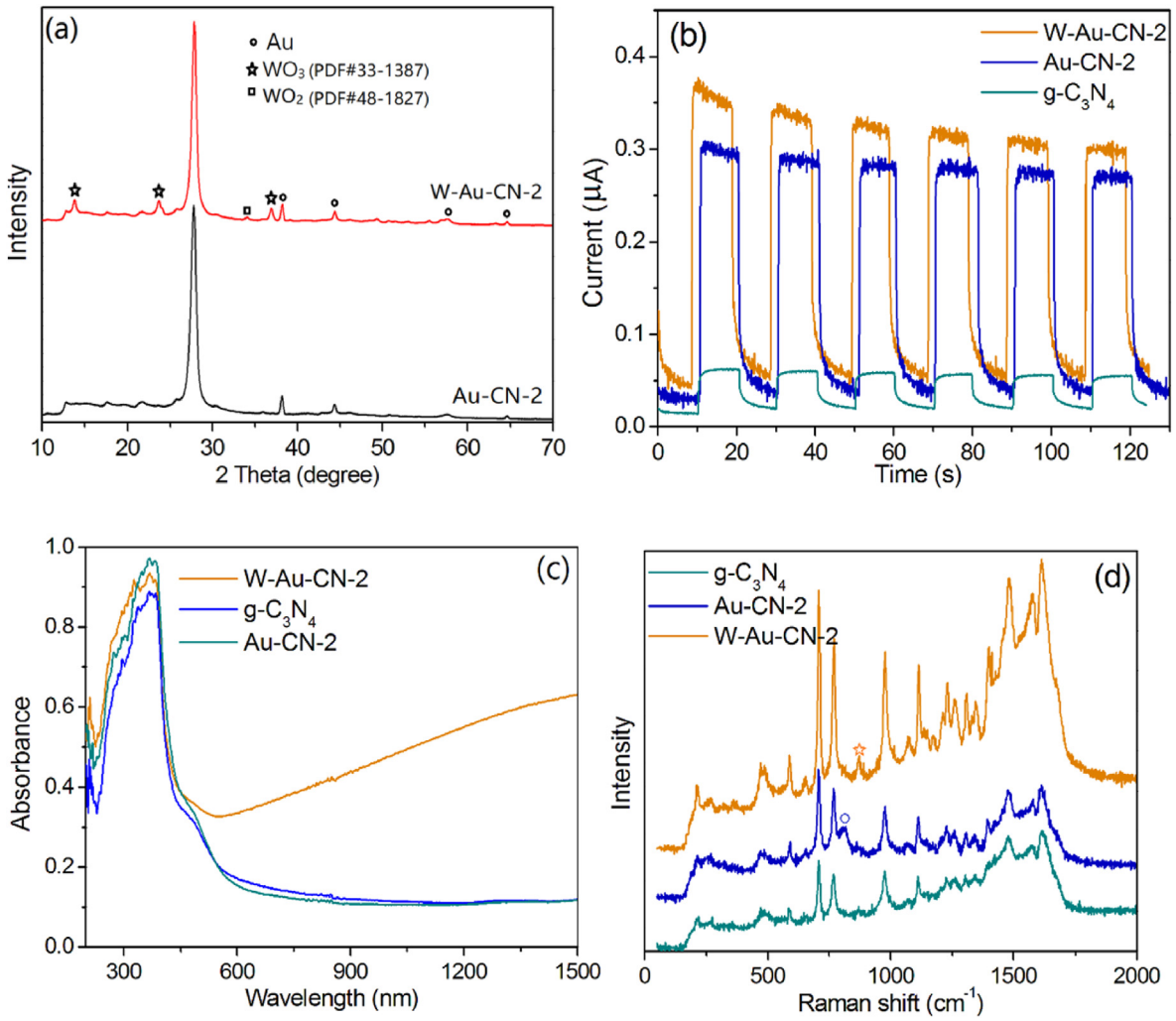

Fig. 4. (a) XRD patterns of the sample W–Au–CN-2 and Au–CN-2. (b) Photo currents of the sample W–Au–CN-2, Au–CN-2 and g-C_3N_4. (c), UV–Vis diffuse reflectance spectra of the samples. (d) Raman spectra of the samples.

Table 2
H_2, CO, and CH_4 evolution performances of samples.

Sample	H_2 (μmol/g/h)	CO (μmol/g/h)	CH_4 (μmol/g/h)
g-C_3N_4	210	n/a	n/a
Au–CN-1	420	0.48	0.30
Au–CN-2	560	0.89	0.56
Au–CN-3	480	0.63	0.42
W–Au–CN-1	3990	3.62	1.78
W–Au–CN-2	5659	5.64	2.58
W–Au–CN-3	4100	4.21	1.32

H_2 evolution was observed for the WO_x and Au modified g-C_3N_4 heterostructure catalysts in comparison with that of Au (only) modified g-C_3N_4 samples. In case of photocatalytic H_2 evolution without using any co-catalyst, the activity of these W–Au–CN catalysts can be considered to be reasonably high compared with other similar literature reported ones. Moreover, sample W–Au–CN-2 also showed quite high H_2 generation stability with no obvious decrease in H_2 evolution observed after 5 cycles of testing (as shown on the cyclic stability test plots in Fig. 5a).

In general, in order for photocatalytic water splitting reactions to occur, the band gap of the heterostructure photocatalyst has to be larger than minimum Gibbs free energy required for water splitting (that is 1.23 V in this case). A valence band maximum that is more positive than the oxygen evolution potential (0.82 V vs NHE at pH = 7, equation (1)), and a conduction band minimum that is more negative than the hydrogen generation potential (−0.41 V vs. NHE, at pH = 7, equation (2)) are required for the heterostructure photocatalyst [45–47].

$$H_2O + 2h^+ \rightarrow O_2 + 2H^+ + 4e^- \quad (1)$$

$$4H^+ + 4e^- \rightarrow 2H_2 \quad (2)$$

The reason that loading of metal co-catalysts is required during photocatalytic measurements is that co-catalysts are often used as photogenerated charge carrier trap sites enhancing charge separation. However, in the case of WO_x/Au-g-C_3N_4 heterostructure composites, no co-catalyst is necessary since Au clusters work as the charge carrier trap sites facilitating H_2 evolution. And the enhanced H_2 generation can be attributed to the formation of these heterostructures in this case. With the WO_x and Au clusters modified g-C_3N_4 heterostructures having more positive valence band maximum and more negative conduction band minimum, the redox capability for a variety of reactions can be enhanced. In addition, the immobilization of WO_x was also able to improve the

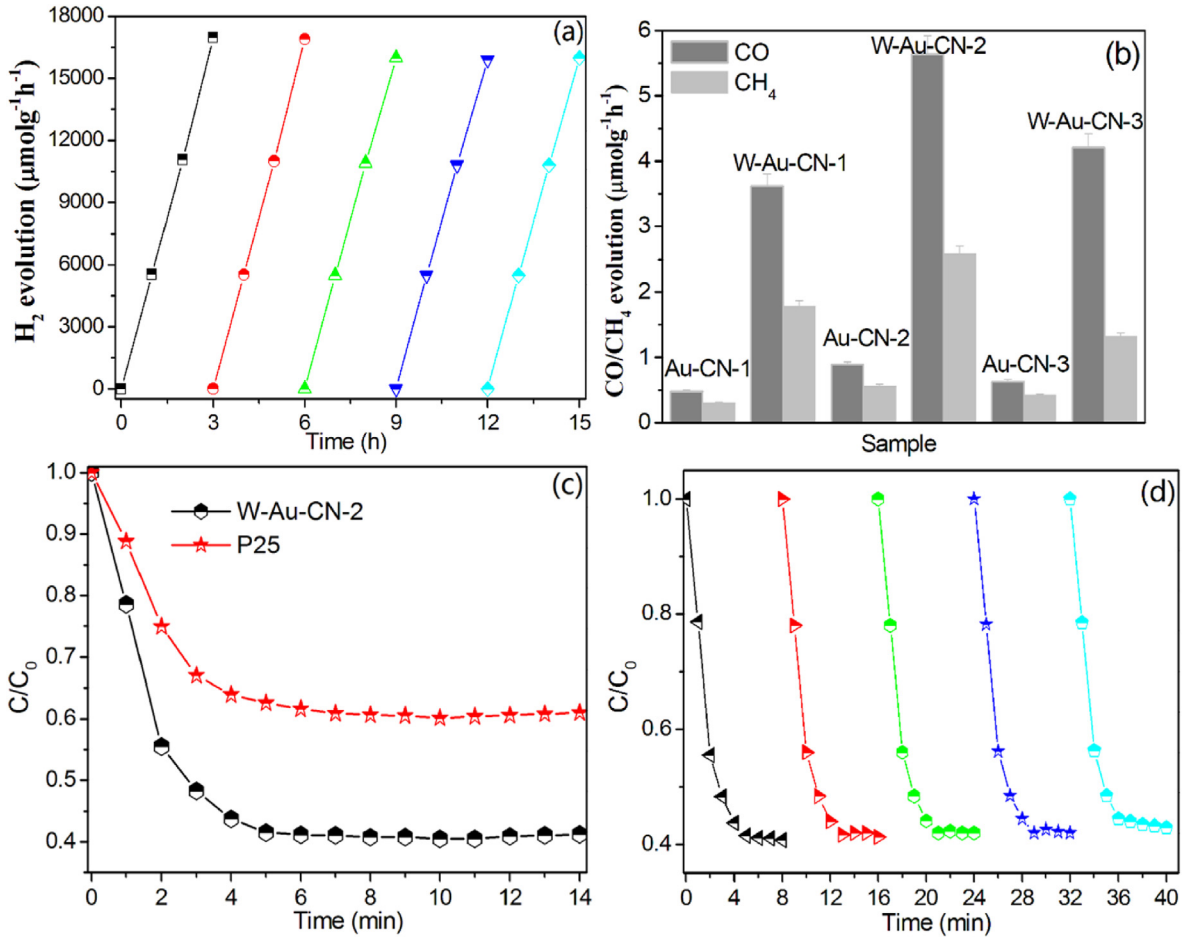

Fig. 5. (a) Time courses of photocatalytic H_2 generation of sample W–Au–CN-2 (five cycles). (b) Comparison on CO and CH_4 evolution performances of the samples under xenon lamp irradiation (full spectrum condition) with no co-catalyst addition. (c) Photocatalytic NO removal rate comparison. (d) Cyclic NO oxidation stability test for sample W–Au–CN-2.

light absorption capability of the heterostructure composites by extending the light-response range of the material to the near infrared region. The detailed photocatalytic mechanism of these heterostructures will be discussed later.

To further investigate the photocatalytic activity of the WO_x/Au-g-C_3N_4 heterostructures, CO_2 photoreduction test was done on the samples and the data are listed in Table 2. CO_2 photoreduction for carbon-based fuel (e.g., methane, carbon monoxide, methanol etc.) production has been hot topics recent years. In order to have the carbon-based fuel evolution reactions (from CO_2 photoreduction) to occur, a more negative conduction band minimum in comparison with that of the standard carbon-based fuel (e.g., CO and CH_4) evolution potential (in V vs. NHE at pH = 7, shown in *eq*. 3 and 4) is often required for the catalysts [48,49].

$$CO_2 + 8\,H^+ + 8e^- \rightarrow CH_4 + 2H_2O\ E^o = -0.24\ V \quad (3)$$

$$CO_2 + 2\,H^+ + 2e^- \rightarrow CO + H_2O\ E^o = -0.52\ V \quad (4)$$

Fig. 5b shows the histogram chart for the comparison of CO and CH_4 evolution rate in full solar spectrum irradiation condition of the Au clusters and WO_x/Au immobilized composite samples and with no co-catalyst addition. In comparison with the extremely poor CO_2 photoreduction performance of pristine g-C_3N_4 nanosheets, a significant increase in CO and CH_4 evolution was observed for the Au clusters modified g-C_3N_4 composites (Au–CN). This is due to the fact that by introducing of Au clusters and WO_x to the g-C_3N_4 network, bandgap narrowing accompanied by the adjustment on the band edge position occurs, leading to extending in light absorption range of the heterostructures. Sample W–Au–CN-2 revealed the best CO and CH_4 evolution performance among all the heterostructure samples with a CO generation rate of 5.64 $\mu molg^{-1}h^{-1}$ and a CH_4 evolution rate of 2.58 $\mu molg^{-1}h^{-1}$. Similar trend was also observed for the photocatalytic H_2 evolution data. The heterostructure nanoarchitectonics of WO_x/Au-g-C_3N_4 is the key in attaining efficient CO_2 photoreduction.

Photocatalytic NO removal test was also performed on the heterostructure samples. NO removal occurs when the photogenerated electrons migrate to the valence band of photocatalyst and react with the O_2 adsorbed on the surface of the material forming $\cdot O^{2-}$ species which can be then used for oxidizing NO into NO_3^-. The detailed reactions are shown as follows (equations (5) and (6))

$$e_{CB}^- + O_2 \rightarrow {}^{\bullet}O_2^- \quad (5)$$

$$NO + {}^{\bullet}O_2^- \rightarrow NO_3^- \quad (6)$$

Fig. 5c shows the NO removal plots obtained for sample W–Au–CN-2 using the NO removal performance data of P25 for comparison. Sample W–Au–CN-2 was able to remove about 61% of the NO within 6 min while P25 was able to remove only 40%. The

NO removal cyclic stability test results obtained for sample W–Au–CN-2 (in Fig. 5d) shows that the NO removal efficiency of sample W–Au–CN-2 remained almost unchanged after 5 cycles. The constructed WO_x/Au-g-C_3N_4 heterostructures can be considered a highly efficient semiconducting photocatalyst that can be used for many photocatalytic applications due to the narrowed bandgap, abundant surface oxygen vacancies (due to the presence of WO_3 and WO_2 in the WO_x component of the heterostructure), extended light absorption range (due to the intense localized surface plasmon resonance absorption of WO_x in both visible and near infrared region) and thus enhanced photocatalysis [50]. The abundant surface oxygen vacancies present on the heterostructures is able to cause collective oscillations of excess charges (electrons) that is similar to that of the localized surface plasmon resonance effect of noble metals, leading to improved photocatalysis. In order to investigate the active species during photocatalytic reactions, quenching experiments for rhodamine B (RhB) photodegradation were performed using WO_x/Au-g-C_3N_4 heterostructures (sample W–Au–CN-2) as the catalyst and $AgNO_3$, disodium salt dihydrate ($EDTA\text{-}Na_2$), benzoquinone (BQ), isopropanol (IPA) as the scavenger to capture e^-, h^+, $\bullet O^{2-}$, •OH, respectively. It was found that $\bullet O^{2-}$, produced in the WO_x/Au-g-C_3N_4 heterostructures system, was the main active species for RhB photodegradation reations. And both $\bullet O^{2-}$ and •OH contribute significantly to improving the photocatalytic activities of the WO_x/Au/g-C_3N_4 heterostructures system.

According to the results obtained, charge transport in WO_x/Au-g-C_3N_4 photocatalyst does not follow the type II mechanism, but a direct solid-state Z-scheme mechanism (as proposed in Scheme 2a) with different charge transfer paths that facilitates charge carrier separation/transfer and enhances photocatalytic performances of the catalyst. There exist three charge transport channels in the WO_x/Au-g-C_3N_4 Z-scheme photocatalytic system involving: electron excitation from valence band to conduction band; electron excitation from valence band to the oxygen vacancies below the conduction band; and electron excitation caused by localized surface plasmon resonance. Au cluster incorporation is the key in switching the interfacial charge transfer routes of g-C_3N_4 and WO_x from type II to direct Z-scheme with electrons in the conduction band of WO_x transported to the valence band of g-C_3N_4. In this case, Au cluster works as the electron sink that can assist capture and transport of the photogenerated electrons, facilitating charge separation and therefore improving the photocatalytic activities.

Benzene oxidation measurement was also performed on the pure g-C_3N_4 nanosheets sample and W–Au-g–CN–2 composites. The pure g-C_3N_4 nanosheets sample could not catalyse benzene-to-phenol oxidation reaction because of its band gap limitations. According to literature, the incorporation of noble metals is often required in this case to facilitate charge transfer from the metallic part of the composite catalyst to the lowest unoccupied molecular orbital of the g-C_3N_4 part in order to catalyse benzene oxidation reactions with the assistant of H_2O_2 [34]. Sample Au-g–CN–2 showed a phenol yield of only 5% in the case of using acetonitrile as the solvent but with no H_2O_2 addition. H_2O_2 can be considered to be one of the key components during the benzene-to-phenol photooxidation reactions since the photo-excited electrons in the conduction band of the catalyst have to be transferred to H_2O_2 to generate hydroxyl radicals that can be used for further oxidation reactions [47]. Under dark condition, the heterostructure sample W–Au-g–CN–2 showed 43.5% of benzene-to-phenol conversion rate and a phenol selectivity of 52.1%. A drastic enhancement in benzene-to-phenol conversion efficiency and selectivity (to phenol) was observed for sample W–Au-g–CN–2 under full solar spectrum light irradiation condition. The selectivity and the conversion rate measured for sample W–Au–CN-2 reached 99.3% and 88.1%, respectively, suggesting the existence of synergistic effects between the Au clusters, WO_x nanocomponents and ultrathin g-C_3N_4 in the heterostructure system. The schematic illustration of the proposed mechanism for benzene photo-oxidation reactions using WO_x/Au-g-C_3N_4 heterostructure photocatalyst under full solar spectrum irradiation condition is shown in Scheme 2b with hydroxyl radicals to be the key active species. The incorporation of homogeneously distributed Au clusters is necessary due to the fact that it can facilitate hydroxyl radical generation in the g–C_3N_4–based composite catalyst system, promote charge transport in-between the g-C_3N_4/WO_x phases and form hydroxy cyclohexadienyl radicals (via reaction between hydroxyl radical and benzene) that works as the key intermediates in initiating further oxidation reaction by reacting with the photogenerated holes for attaining phenol production [48,51].

4. Conclusion

To have control over the thermal polymerization reactions, a mechano-chemical pre-treatment process was applied to incorporate Au clusters into g-C_3N_4 nanosheets base. Small Au NPs and clusters were homogeneously embedded in ultrathin g-C_3N_4. The Au modified g-C_3N_4 nanosheets showed enhanced photocurrent generation which also in consistency with the photocatalytic performances results (H_2 generation and CO_2 reduction). A solvothermal synthesis method was applied to incorporate WO_x nanobelts on the Au modified g-C_3N_4. WO_x nanobelts with abundant oxygen vacancies were decorated on Au-modified g-C_3N_4 nanosheets to form the two dimensional (2D)/2D WO_x/Au-g-C_3N_4 heterojunctions having excellent CO_2 photo-reduction

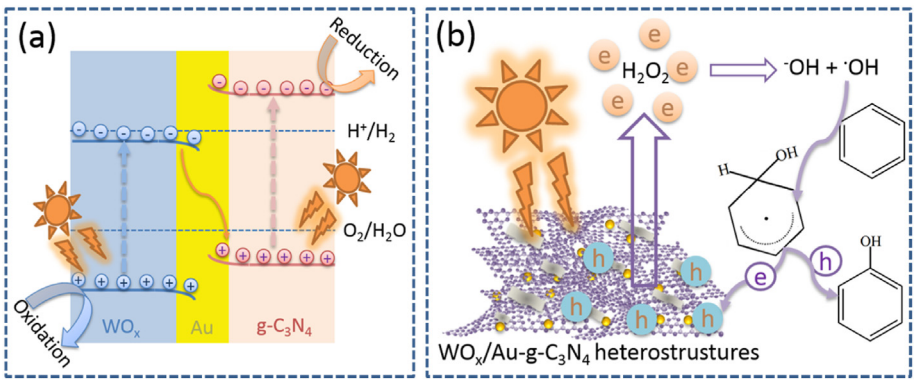

Scheme 2. (a) Schematic diagram of electron transport in Z-scheme photocatalytic system. (b) Proposed mechanism for catalytic benzene oxidation using WO_x-Cu-g-C_3N_4 heterojunctions under light irradiation.

performances in full solar spectrum condition (with a CO and CH_4 generation rate of 5.64 and 2.58 $\mu molg^{-1}h^{-1}$, respectively). The presence of Au clusters in the heterostructure system (constructed using the idea of nanoarchitectonics) is the key that leads to the double Z-scheme charge transport system formation with improved charge separation/transport efficiency due to the built-up direct Z-scheme charge transfer between Au and g-C_3N_4 (or WO_x) as well as the indirect charge transfer between WO_x and g-C_3N_4. The NO removal rate of the WO_x/Au-g-C_3N_4 heterojunctions with optimized composition ratio reached 61%. This work may contribute to offer novel strategies for the design of hierarchical g-C_3N_4 hybrid nanostructures that can be used as promising photocatalysts for solar energy conversion and pollutant treatment. The constructed WO_x/Au-g-C_3N_4 heterojunctions catalyst showed outstanding benzene to phenol conversion rate (88.1%) and excellent selectivity (99.3%) under full solar spectrum irradiation as well as high stability and cyclability, possessing huge potential in direct conversion of benzene to phenol.

Credit author statement

Xiao Zhang: Conceptualization, Methodology, Investigation, Writing – original draft, Writing – review & editing. Katarzyna Matras-Postolek: Writing – review & editing. Ping Yang: Investigation, Writing – review & editing.

Declaration of competing interest

The authors declare that they have no known competing financial interests or personal relationships that could have appeared to influence the work reported in this paper.

Data availability

Data will be made available on request.

Acknowledgements

This research is part of the project No. 2021/43/P/ST5/01729 co-funded by the National Science Centre and the European Union Framework Programme for Research and Innovation Horizon 2020 under the Marie Skłodowska-Curie grant agreement No. 945339  . For the purpose of Open Accesss, the author has applied a CC-BY public copyrght license to any Author Accepted Manuscript (AAM) version arising from this submission. This work was also supported partly by the National Natural Science Foundation of China, China (grant no. 51972145), Ji Nan Science & Technology Bureau, China (No. 2019GXRC016 and 2021GXRC109), and University of Jinan, China (XKY2118).

References

[1] J. Ran, M. Jaroniec, S.Z. Qiao, Cocatalyst in semiconductor-based photocatalytic CO_2 reduction: achievements, challenges, and opportunities, Adv. Mater. 30 (2018), 1704649.
[2] S. Bai, Q. Shao, P. Wang, Q. Dai, X. Wang, X. Huang, Highly active and selective hydrogenation of CO_2 to ethanol by ordered Pd-Cu NPs, J. Am. Chem. Soc. 139 (2017) 6827–6830.
[3] J. Ran, J. Zhang, J. Yu, M. Jaroniec, S. Qiao, Earth-abundant cocatalysts for semiconductor based photocatalytic water splitting, Chem. Soc. Rev. 43 (2014) 7787–7812.
[4] X. Zhang, P. Yang, S.P. Jiang, Ni diffusion in vertical growth of MoS_2 nanosheets on carbon nanotubes towards highly efficient hydrogen evolution, Carbon 175 (2021) 176–186.
[5] B. Shao, Z. Liu, G. Zeng, Z. Wu, Y. Liu, M. Cheng, M. Chen, Y. Liu, W. Zhang, H. Feng, Nitrogen-doped hollow mesoporous carbon spheres modified g-C_3N_4/Bi_2O_3 direct dual semiconductor photocatalytic system with enhanced antibiotics degradation under visible light, ACS Sustain. Chem. Eng. 6 (2018) 16424–16436.
[6] K. Maeda, T.E. Mallouk, Two-dimensional metal oxide nanosheets as building blocks for artificial photosynthetic assemblies, Bull. Chem. Soc. Jpn. 92 (2019) 38–54.
[7] Z. Jiang, X. Zhang, J. Wang, L. Chen, H.-S. Chen, P. Yang, Ultrastable g-C_3N_4 assemblies with high quantum yield and revisable photoluminescence, Chem. Commun. 54 (2018) 13519–13522.
[8] N.R. Glavin, R. Rao, V. Varshney, E. Bianco, A. Apte, A. Roy, E. Ringe, P.M. Ajayan, Emerging applications of elemental 2D materials, Adv. Mater. 32 (2020), 1904302.
[9] X. Zhang, S. He, S.P. Jiang, WO_x/g-C_3N_4 layered heterostructures with controlled crystallinity towards superior photocatalytic degradation and H_2 generation, Carbon 156 (2020) 488–498.
[10] Y. Wang, X. Wang, M. Antonietti, Polymeric graphitic carbon nitride as a heterogeneous organocatalyst: from photochemistry to multipurpose catalysis to sustainable chemistry, Angew. Chem. Int. Ed. 51 (2012) 68–89.
[11] X. Wang, K. Maeda, A. Thomas, K. Takanabe, G. Xin, J. Carlsson, K. Domen, M. Antonietti, A metal-free polymeric photocatalyst for hydrogen production from water under visible light, Nat. Mater. 8 (2009) 76–80.
[12] J. Liu, H. Wang, M. Antonietti, Graphitic carbon nitride "reloaded": emerging applications beyond (photo)catalysis, Chem. Soc. Rev. 45 (2016) 2308–2326.
[13] J. Li, S. Zhao, S. Yang, S. Wang, H. Sun, S.P. Jiang, B. Johannessen, S. Liu, Atomically dispersed cobalt on graphitic carbon nitride as robust catalyst for selective oxidation of ethylbenzene by peroxymonosulfate, J. Mater. Chem. 9 (2021) 1–7.
[14] X. Zhang, X.R. Zhang, P. Yang, H.S. Chen, S.P. Jiang, Black magnetic Cu-g-C_3N_4 nanosheets for efficiently photocatalytic H_2 generation and CO_2/benzene conversion, Chem. Eng. J. 450 (2022), 138030.
[15] M.B. Zakaria, C. Li, Q. Ji, B. Jiang, S. Tominaka, Y. Ide, J.P. Hill, K. Ariga, Y. Yamauchi, Self-construction from 2D to 3D: one-pot layer-by-layer assembly of graphene oxide sheets held together by coordination polymers, Angew. Chem. Int. Ed. 55 (2016) 8426–8430.
[16] X. Zhang, P. Wang, P. Yang, S.P. Jiang, Photo-chemical property evolution of superior thin g-C_3N_4nanosheets with their crystallinity and Pt deposition, Int. J. Hydrogen Energy 45 (2020) 21523–21531.
[17] X. Zhang, J.P. Veder, S. He, S.P. Jiang, Construction of 2D g-C_3N_4 lateral-like homostructures and their photo- and electro-catalytic activities, Chem. Commun. 55 (2019) 1233–1236.
[18] X. Zhang, P. Yang, S.P. Jiang, Pt NPs embedded spine-like g-C_3N_4 cages with superior photocatalytic activity for H_2 generation and CO_2 reduction, Nanotechnology 32 (2021), 175401.
[19] S. Wang, J. Zhang, B. Li, H. Sun, S. Wang, Engineered graphitic carbon nitride-based photocatalysts for visible-light-driven water splitting: a review, Energy Fuel. 35 (2021) 6504–6526.
[20] N. Roy, N. Suzuki, C. Terashima, A. Fujishima, Recent improvements in the production of solar fuels: from CO_2 reduction to water splitting and artificial photosynthesis, Bull. Chem. Soc. Jpn. 92 (1) (2019) 178–192.
[21] C.N.R. Rao, K. Pramoda, BxCyNz Borocarbonitrides, 2D nanocomposites with novel properties, Bull. Chem. Soc. Jpn. 92 (2019) 441–468.
[22] Y. Zhu, Z. Xu, Q. Lang, W. Jiang, Q. Yin, S. Zhong, S. Bai, Grain boundary engineered metal nanowire cocatalysts for enhanced photocatalytic reduction of carbon dioxide, Appl. Catal. B Environ. 206 (2017) 282–292.
[23] X. Zhang, X.R. Zhang, P. Yang, S.P. Jiang, Transition metals decorated g-C_3N_4/N-doped carbon nanotube catalysts for water splitting: a review, J. Electroanal. Chem. 895 (2021), 115510.
[24] X. Zhang, P. Yang, S.P. Jiang, Edge-epitaxial growth of layered yellow g-C_3N_4 on red g-C_3N_4 nanosheets and their superior photocatalytic activities, Chem. Commun. 57 (2021) 3119–3122.
[25] Z. Jiang, X. Zhang, H.S. Chen, P. Yang, S.P. Jiang, Fusiform-shaped g-C_3N_4 capsules with superior photocatalytic activity, Small 16 (2020), 2003910.
[26] T. Song, X. Zhang, P. Yang, Bifunctional nitrogen-doped carbon dots in g-C_3N_4/WO_x heterojunction for enhanced visible-light photocatalytic water splitting performance, Langmuir 37 (2021) 4236–4247.
[27] Y. Li, Z. Tang, J. Zhang, Z. Zhang, Defect engineering of air treated WO_3 and its enhanced visible-light-driven photocatalytic and electrochemical performance, J. Phys. Chem. C 120 (2016) 9750–9763.
[28] J. Meng, Q. Lin, T. Chen, X. Wei, J. Li, Z. Zhang, Oxygen vacancy regulation on tungsten oxides with specific exposed facets for enhanced visible-light-driven photocatalytic oxidation, Nanoscale 10 (2018) 2908–2915.
[29] M. Liu, S. Wageh, A.A. Al-Ghamdi, Pe Xia, B. Cheng, L. Zhang, J. Yu, Quenching induced hierarchical 3D porous g-C_3N_4 with enhanced photocatalytic CO_2 reduction activity, Chem. Commun. 55 (2019) 14023–14026.
[30] K. Zhu, X. Luan, K. Matras-Postolek, P. Yang, 2D/2D MoS_2/g-C_3N_4 layered heterojunctions with enhanced interfacial electron coupling effect, J. Electroanal. Chem. 893 (2021), 115350.
[31] Y. Ren, Q. Han, Y. Zhao, H. Wen, Z. Jiang, The exploration of metal-free catalyst g-C_3N_4 for NO degradation, J. Hazard Mater. 404 (2021), 124153.
[32] J. Lin, W. Tian, H. Zhang, X. Duan, H. Sun, S. Wang, Graphitic carbon nitride-based Z-scheme structure for photocatalytic CO_2 reduction, Energy Fuel. 35 (2021) 7–24.
[33] L. Lin, Z. Yu, X. Wang, Crystalline carbon nitride semiconductors for photocatalytic water splitting, Angew. Chem. Int. Ed. 58 (2019) 6164–6175.
[34] S. Mahdi Hosseini, M. Ghiaci, S.A. Kulinich, W. Wunderlich, H. Farrokhpour, M. Saraji, A. Shahvar, Au-Pd@g-C_3N_4 as an efficient photocatalyst for visible-

light oxidation of benzene to phenol: experimental and mechanistic study, J. Phys. Chem. C 122 (2018) 27477–27485.
[35] K. Ariga, Nanoarchitectonics: what's coming next after nanotechnology, Nanoscale Horiz 6 (2021) 364–378.
[36] K. Ariga, Y. Yamauchi, Nanoarchitectonics from atom to life, Chem. Asian J. 15 (2020) 718–728.
[37] K. Ariga, J. Li, J. Fei, Q. Ji, J.P. Hill, Nanoarchitectonics for dynamic functional materials from atomic-/molecular-level manipulation to macroscopic action, Adv. Mater. 28 (2016) 1251–1286.
[38] B.N. Bhadra, L.K. Shrestha, K. Ariga, Porous carbon nanoarchitectonics for the environment: detection and adsorption, CrystEngComm 24 (2022) 6804–6824.
[39] Z. Jiang, C. Jia, B. Wang, P. Yang, G. Gao, Hexagonal g-C_3N_4 nanotubes with Pt decorated surface towards enhanced photo- and electro-chemistry performance, J. Alloys Compd. 826 (2020), 154145.
[40] L. Shi, Z. Li, K. Marcus, G. Wang, K. Liang, W. Niu, Y. Yang, Integration of Au, nanoparticles with a g-C_3N_4 based heterostructure: switching charge transfer from type-II to Z-scheme for enhanced visible light photocatalysis, Chem. Commun. 54 (2018) 3747–3750.
[41] T. Song, C. Xie, K. Matras-Postolek, P. Yang, 2D layered g-C_3N_4/WO_3/WS_2 heterojunctions with enhanced photochemical performance, J. Phys. Chem. C 125 (2021) 19382–19393.
[42] D. Liu, S. Zhang, J. Wang, T. Peng, R. Li, Direct Z-scheme 2D/2D photocatalyst based on ultrathin g-C_3N_4 and WO_3 nanosheets for efficient visible-light-driven H_2 generation, ACS Appl. Mater. Interfaces 11 (2019) 27913–27923.
[43] Y. Wei, X. Zhang, Z. Liu, H.S. Chen, P. Yang, Site-selective modification of AgPt on multibranched Au nanostars for plasmon-enhanced hydrogen evolution and methanol oxidation reaction in visible to near-infrared region, J. Power Sources 425 (2019) 17–26.
[44] Z. Guo, Y. Xie, J. Xiao, Z.J. Zhao, Y. Wang, Z. Xu, Y. Zhang, L. Yin, H. Cao, J. Gong, Single-atom Mn-N_4 site-catalyzed peroxone reaction for the efficient production of hydroxyl radicals in an acidic solution, J. Am. Chem. Soc. 141 (2019) 12005–12010.
[45] X. Zhang, X. Zhang, P. Yang, S.P. Jiang, Pt clusters embedded in g-C_3N_4 nanosheets to form Z-scheme heterostructures with enhanced photochemical performance, Surface. Interfac. 27 (2021), 101450.
[46] X. Zhang, X. Zhang, P. Yang, S.P. Jiang, Layered graphitic carbon nitride: synthesis, photo/electro chemical performance and trends, J. Nanostr. Chem. 12 (2022) 669–691.
[47] Z. Liu, X. Zhang, Z. Jiang, H.S. Chen, P. Yang, Phosphorus and sulphur co-doping of g-C_3N_4 nanotubes with tunable architectures for superior photocatalytic H_2 evolution, Int. J. Hydrogen Energy 44 (2019) 20042–20055.
[48] X. Cai, A. Wang, J. Wang, R. Wang, S. Zhong, Y. Zhao, L. Wu, J. Chen, S. Bai, Order engineering on the lattice of intermetallic Pd Cu co-catalysts for boosting the photocatalytic conversion of CO_2 into CH_4, J. Mater. Chem. 6 (2018) 17444–17456.
[49] V. Kumaravel, J. Bartlett, S.C. Pillai, Photoelectrochemical conversion of carbon dioxide (CO_2) into fuels and value-added products, ACS Energy Lett. 5 (2020) 486–519.
[50] C. Jia, X. Zhang, K. Matras-Postolek, B. Huang, P. Yang, Z-scheme rGO/TiO_2-Bronze/$W_{18}O_{49}$ ternary heterostructure towards efficient full solar-spectrum photocatalysis, Carbon 139 (2018) 415–426.
[51] G. Liao, S. Chen, X. Quan, H. Yu, H. Zhao, Graphene oxide modified g-C_3N_4 hybrid with enhanced photocatalytic capability under visible light irradiation, J. Mater. Chem. 22 (2012) 2721–2726.